

Enhanced Optical Emission from 2D InSe Bent onto Si-Pillars

Debarati Mazumder, Jiahao Xie, Zakhar R. Kudrynskyi, Xinjiang Wang, Oleg Makarovskiy, Mahabub A. Bhuiyan, Hyunseok Kim, Ting-Yuan Chang, Diana L. Huffaker, Zakhar D. Kovalyuk, Lijun Zhang,* and Amalia Patanè*

Controlling the propagation and intensity of an optical signal is central to several technologies ranging from quantum communication to signal processing. These require a versatile class of functional materials with tailored electronic and optical properties, and compatibility with different platforms for electronics and optoelectronics. Here, the inherent optical anisotropy and mechanical flexibility of atomically thin semiconducting layers are investigated and exploited to induce a controlled enhancement of optical signals. This enhancement is achieved by straining and bending layers of the van der Waals crystal indium selenide (InSe) onto a periodic array of Si-pillars. This enhancement has strong dependence on the layer thickness and is modelled by first-principles electronic band structure theory, revealing the role of the symmetry of the atomic orbitals and light polarization dipole selection rules on the optical properties of the bent layers. The effects described in this paper are qualitatively different from those reported in other materials, such as transition metal dichalcogenides, and do not arise from a photonic cavity effect, as demonstrated before for other semiconductors. The findings on InSe offer a route to flexible nano-photonics compatible with silicon electronics by exploiting the flexibility and anisotropic and wide spectral optical response of a 2D layered material.

range of quantum phenomena.^[1,2] These 2D crystals have strong covalent atomic bonding in the layer planes and vdW attraction between the layers, enabling the exfoliation from bulk crystals of high-quality thin films with tailored electronic and optical properties. Within the vast family of vdW crystals, the search for transformative materials beyond graphene has led to the rapidly growing development of the metal chalcogenide indium selenide, InSe. This 2D semiconductor has a band gap energy that increases markedly with decreasing layer thickness down to a single layer,^[3–7] resulting into a high, broad photoresponsivity that extends from the ultraviolet (UV) to the infrared (IR) range.^[8–11] Furthermore, the low effective mass of the conduction band (CB)^[6] leads to a high room temperature electron mobility, larger than that in Si-based field effect transistors.^[6,12,13] These properties make InSe an ideal compromise between semiconducting Si and high-mobility graphene for 2D digital electronics and optoelectronics.


1. Introduction

Atomically thin layers of van der Waals (vdW) crystals and their heterostructures offer opportunities to study and exploit a wide

The fundamental science of 2D InSe is an exciting research field with recent breakthroughs emerging from its unique electronic band structure. This differs qualitatively from that of many other 2D materials, such as the widely studied transition

D. Mazumder, Dr. Z. R. Kudrynskyi, Dr. O. Makarovskiy, Dr. M. A. Bhuiyan, Prof. A. Patanè
School of Physics and Astronomy
University of Nottingham
Nottingham NG7 2RD, UK
E-mail: amalia.patane@nottingham.ac.uk

J. Xie, Dr. X. Wang, Prof. L. Zhang
State Key Laboratory of Integrated Optoelectronics
Key Laboratory of Automobile Materials of MOE
College of Materials Science and Engineering
Jilin University
Changchun 130012, China
E-mail: lijun_zhang@jlu.edu.cn

 The ORCID identification number(s) for the author(s) of this article can be found under <https://doi.org/10.1002/adom.202000828>.

© 2020 The Authors. Published by WILEY-VCH Verlag GmbH & Co. KGaA, Weinheim. This is an open access article under the terms of the Creative Commons Attribution License, which permits use, distribution and reproduction in any medium, provided the original work is properly cited.

DOI: 10.1002/adom.202000828

Dr. H. Kim, T.-Y. Chang, Prof. D. L. Huffaker
Department of Electrical and Computer Engineering
University of California
Los Angeles, CA 90095, USA

Prof. D. L. Huffaker
School of Physics and Astronomy
Cardiff University
Cardiff, Wales CF24 3AA, UK

Prof. Z. D. Kovalyuk
Institute for Problems of Materials Science
The National Academy of Sciences of Ukraine
Chernivtsi Branch
Chernivtsi 58001, Ukraine

metal dichalcogenides (TMDCs): the CB edge states of InSe arise from antibonding In *s*-states, whereas the top valence band (VB) consists of Se *p_z*-like orbitals.^[4,14,15] Thus, band edge excitons tend to couple preferentially to light polarized along the *z*-direction (or *c*-axis), rather than along the *xy*-plane as for TMDCs.^[4] Mechanical strain can modify these properties.^[16–20] 2D vdW crystals can sustain high strain in reversible fashion due to their large mechanical flexibility^[21–23] and, amongst them, InSe is one of the most flexible systems with a small Young's modulus (23.1 ± 5.2 GPa)^[24] and a bandgap energy that is very sensitive to strain.^[25] Thus, InSe represents a promising system to explore and exploit the effects of strain on electronic and optical properties.

Here, we report on the modulation of the optical properties of atomically thin InSe layers under controllable bending conditions achieved by exfoliation and transfer of InSe flakes onto a periodic array of Si-pillars. We show a site-specific, reproducible bending of individual flakes onto the pillars and corresponding enhancement of the Raman and photoluminescence (PL) signals. We explain these findings by first-principles calculations of the electronic band structure of 2D InSe, revealing the role of the strain and geometrical shape of the bent flakes. Our approach to this optical enhancement differs from previous works that used randomly distributed nanoparticles or wrinkles to texture the layers.^[14,15] The effects described in this paper are also qualitatively different from those reported in other materials: they do not arise from localization of carriers and/or non-homogeneous strain intentionally created by transferring the layers onto dielectric pillars; and they do not arise from a photonic cavity effect, that is, from light interactions with sub-wavelength dielectric cavities. Our studies of bent InSe layers with a well-defined geometry demonstrate how the orbital symmetry of the band-edge states and light polarization dipole selection rules affect the optical enhancement for different layer thickness and/or bending. The measured enhancement of the optical signal by more than a factor of 10 in the thinnest layers (≈ 2 nm) offers a route to the controlled modulation of the optical properties of atomically thin semiconductors for flexible optoelectronics, compatible with complementary metal oxide semiconductor technology and planar optical waveguides.

2. Results and Discussion

2.1. Fabrication and Topography of Multiple InSe Layers Bent on Si-Nanopillars

Figure 1a shows our fabrication method to bend thin InSe layers onto a periodic array of Si pillars. The InSe flakes are first mechanically exfoliated from a Bridgman-grown bulk crystal of γ -InSe onto a polydimethylsiloxane (PDMS) film. The PDMS/InSe film is then loaded onto a micromanipulator and transferred onto the pre-patterned Si-substrate. Finally, the PDMS is mechanically peeled off. Figure 1b,c shows scanning electron microscopy (SEM) images of the pre-patterned Si-substrate. The Si-pillars are patterned using electron beam lithography (EBL) and dry etching (see Section 4). They are equally spaced by a distance $d = 3$ μ m and have an average height, $h = 120$ nm, and width, $w = 120$ nm.

InSe layers of different thickness t were identified by optical microscopy (Figure S1, Supporting Information) and SEM, and then transferred onto the pillars. Figure 1d,e shows the SEM images of a bulk InSe flake ($t > 20$ nm) over a periodic Si-pillar array, revealing brighter spots at the location of the pillars. SEM images acquired by viewing the InSe flake at a tilt angle of 40° to the electron beam (Figure 1f) indicate that the flake is tensed over each pillar with a bending that extends over a radial distance of approximately ≈ 500 nm. We observe similar SEM images for atomically thin InSe layers, as shown in Figure 1g–i for an InSe flake with $t = 5$ nm. We obtain the topography of the bent layers by atomic force microscopy (AFM). Figure 1l,m shows AFM images and the height line profile for the same InSe flake imaged by SEM in Figure 1i. The bent flake has a nearly round base; its maximum height, z_0 , is reached at the centre (r_0) of the pillar and corresponds approximately to the pillar height h . The height line profile is well reproduced by a Gaussian profile, that is, $z = z_0 \exp[-(r-r_0)^2/2b^2]$, where $b = 425$ nm and $z_0 = h = 118$ nm (Figure 1m). A similar profile was obtained for thicker InSe flakes ($t > 20$ nm) (Figure S2, Supporting Information). The bending of the flakes can be varied by changing the height of the nanopillars (Figure S2, Supporting Information). For example, for shorter pillars ($h = 64$ nm), the height line profile is described by a Gaussian with $b = 260$ nm and $z_0 = h = 64$ nm. The reproducible topography of the bent flakes on different pillars within an array demonstrates that the method of fabrication is reliable, suggesting that the shape of the bent flakes is determined primarily by the elastic properties of InSe and its good adhesion to Si due to attractive vdW interactions.

2.2. Nanoscale Spatial Modulation of Raman and Photoluminescence Signals

We have conducted PL and Raman studies of InSe flakes of different thickness t . The value of t was determined prior to the transfer of the flake onto the Si-pillars by microPL (μ PL) spectroscopy using a confocal microscope. The room temperature ($T = 300$ K) PL peak energy, E_{PL} , is due the band-edge exciton and is very sensitive to the layer thickness: it increases from $E_{\text{PL}} = 1.25$ eV for $t > 20$ nm to $E_{\text{PL}} = 1.72$ eV for $t = 2$ nm; correspondingly, the intensity of the PL signal decreases markedly as t is decreased below $t = 10$ nm due to an direct-indirect band gap crossover.^[5,6] Figure 2a shows representative room temperature μ PL spectra and the color maps of the PL and Raman intensity for an InSe flake with $t = 9$ nm. An enhancement of both PL and Raman signals can be clearly seen at the position of the Si-pillar. The pillars are well separated from each other and the width (≈ 100 nm) of each pillar is smaller than the wavelength (≈ 1000 nm) of the emitted photons. Thus, an InSe layer bent onto the pillar acts effectively as a point-like source whose submicron size is limited by light diffraction. Due to the small width of the pillars, it is not possible to resolve the spatial distribution of the light intensity within each pillar.

First, we examine the PL spectra of flakes with different thickness t (Figure 2b). These experiments were conducted with incident light polarized in the layer plane and using a back scattering geometry. We used a laser excitation energy of

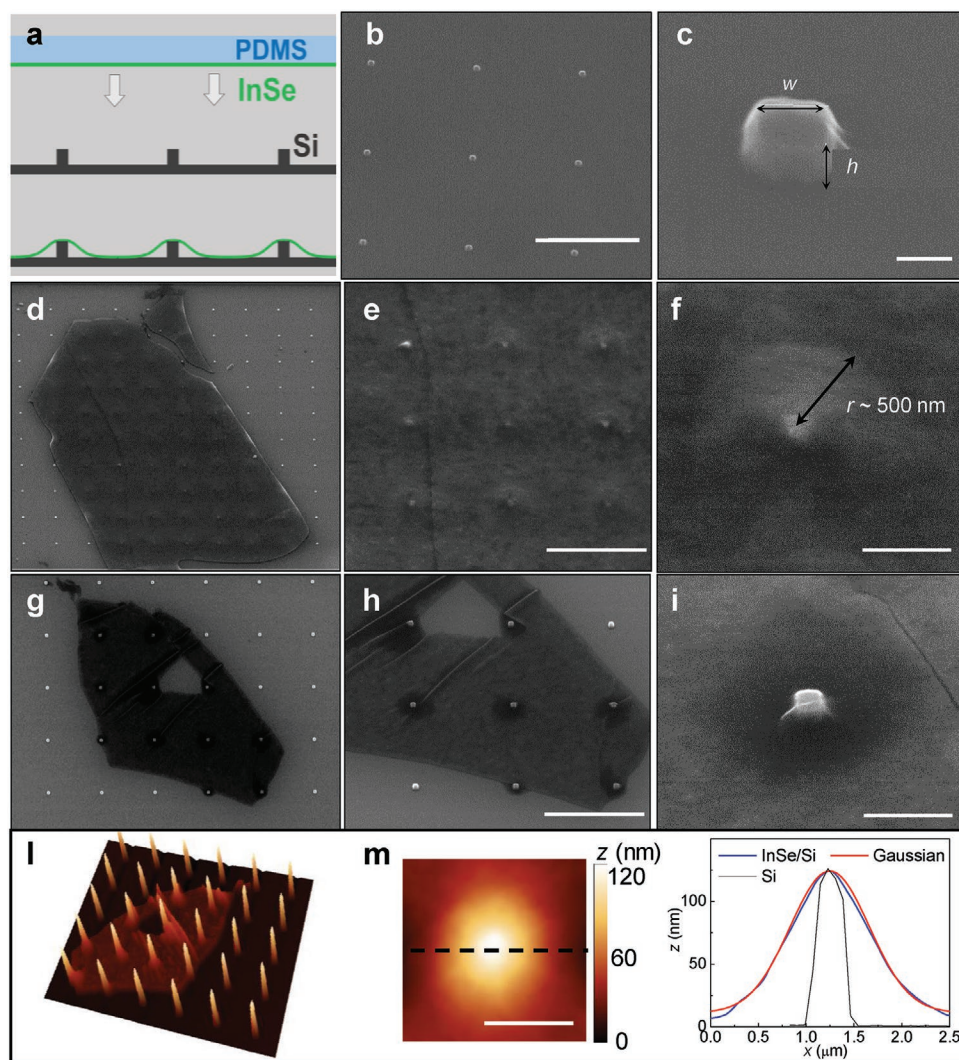


Figure 1. InSe layers on a periodic array of Si-pillars. a) Two-step fabrication: i) Mechanical exfoliation of an InSe flake on PDMS followed by ii) all-dry transfer of the flake on a periodic array of Si-pillars. b,c) SEM images of Si-pillars (width w ; height h). Scale bar: b) $3\ \mu\text{m}$ and c) $100\ \text{nm}$. d-f) SEM images of a bulk InSe flake ($t > 20\ \text{nm}$) on Si-pillars. Scale bar: e) $3\ \mu\text{m}$ and f) $500\ \text{nm}$. g-i) SEM images of an InSe flake ($t = 5\ \text{nm}$) on Si-pillars. Scale bar: h) $3\ \mu\text{m}$ and i) $500\ \text{nm}$. j) 3D AFM image of the InSe flake shown in part (g). m) 2D AFM image and height line profile (blue: data; red: Gaussian fit) for an InSe flake over a Si-pillar. For comparison, the height profile for a Si-pillar is also shown (black). Scale bar: $1\ \mu\text{m}$.

$E_{\text{exc}} = 2.33\ \text{eV}$ ($\lambda = 532\ \text{nm}$) close to the energy of the interband optical transition ($E_2 = 2.4\ \text{eV}$) between the p_{xy} -like orbitals in the VB and the s -like CB states of bulk γ -InSe.^[7] Compared to the band-edge exciton energy, E_g , the energy of the E_2 transition depends less strongly on the layer thickness and increases only when t is reduced below $t = 5\ \text{nm}$.^[7] The PL intensity enhancement ratio, $I_{\text{on}}/I_{\text{out}}$, depends on the thickness of the flake with values ranging from $I_{\text{on}}/I_{\text{out}} = 2$ for bulk flakes ($t > 20\ \text{nm}$) to $I_{\text{on}}/I_{\text{out}} > 10$ for thin flakes with $t = 2\ \text{nm}$ (Figure 2b). The μPL spectra in Figure 2a,b show that the PL peak energy is only slightly red-shifted ($< 5\ \text{meV}$) at the site of the pillar. Figure 2c,d shows the data of $I_{\text{on}}/I_{\text{out}}$ versus photon energy (Figure 2c) and t (Figure 2d), as obtained for InSe layers bent on single pillars. These illustrate that the PL enhancement is significantly larger for $t < 5\ \text{nm}$ (or PL peak energy $E > 1.6\ \text{eV}$).

The scatter in the data of Figure 2c,d suggests that the PL properties of the bent flakes could also be influenced by crystal

defects (e.g., ruptures, wrinkles, etc). For example, although the μPL is always enhanced on the pillars, the PL enhancement can vary across the array. This can be seen in the inset of Figure 2c showing the overlap between an optical image of an InSe flake after its transfer over the pillars and the corresponding color map of the μPL intensity. Furthermore, the PL studies at low temperature ($T = 8\ \text{K}$) indicate an enhancement of the PL emission on the pillars, although less pronounced than at RT (Figure S3 and S4, Supporting Information). At low T , the PL emission is broad both within and outside the pillars and originates from carrier recombination from localized states due to native dopants and donor-acceptor pairs.^[26–28]

The spatial modulation of the PL signal is accompanied by a corresponding variation of the Raman signal. Figure 3a shows representative Raman spectra for flakes of thickness $t = 5\ \text{nm}$, $t = 9\ \text{nm}$ and $t > 20\ \text{nm}$ at different locations, inside and outside a pillar. The Raman signal decreases with decreasing layer thickness

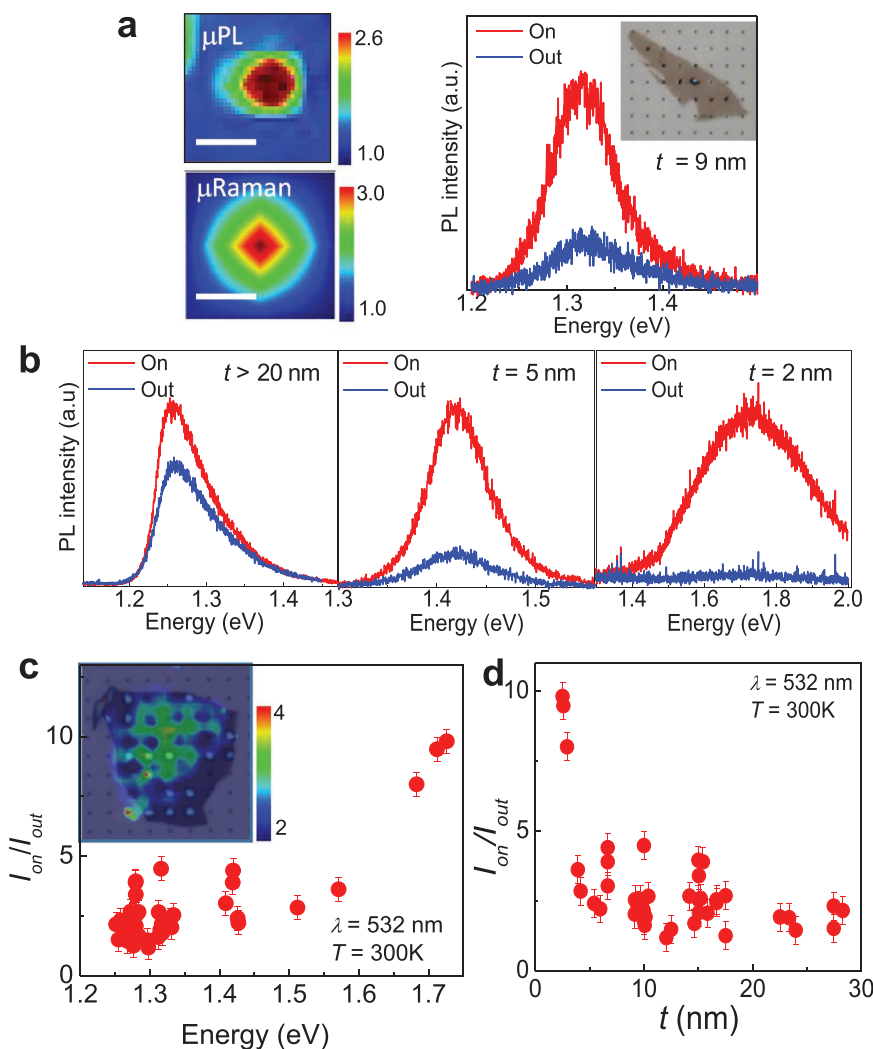


Figure 2. Enhanced optical emission from InSe on Si-pillars. a) Color maps of the micro-photoluminescence (μ PL) and μ Raman intensity for an InSe flake ($t = 9$ nm) on a Si-pillar (scale bar = 2 μ m). The PL intensity is mapped at an energy $E = 1.31$ eV corresponding to the peak energy of the PL spectrum ($\lambda = 633$ nm, $P = 10^{-6}$ W). The μ Raman intensity is integrated over the frequency range $\nu = 100\text{--}300$ cm^{-1} ($\lambda = 532$ nm, $P = 10^{-6}$ W). The corresponding μ PL spectra inside (ON) and outside (OUT) the pillar are shown in the right inset. b) Room temperature μ PL spectra inside and outside a Si-pillar for flakes of thickness from $t = 2$ nm to $t > 20$ nm ($\lambda = 532$ nm, $P = 10^{-6}$ W). c) Ratio $I_{\text{on}}/I_{\text{out}}$ of the PL intensities in and outside Si-pillars of average height $h = 120$ nm versus the PL peak energy for InSe flakes of different thickness t ($T = 300$ K, $\lambda = 532$ nm, $P = 10^{-6}$ W). Inset: optical image of an InSe flake ($t = 18$ nm) on a Si-pillars array overlapped onto the color map of the μ PL intensity (scale bar = 3 μ m). d) Dependence of $I_{\text{on}}/I_{\text{out}}$ on t .

due a reduced absorption coefficient and no Raman signal could be detected for $t < 5$ nm. The Raman spectra reveal distinctive modes peaked at 116, 176, 201, and 228 cm^{-1} . These correspond to the $A_1'(\Gamma_1^2)$, $E'(\Gamma_3^1)\text{-TO}/E''(\Gamma_3^3)$, $A_2''(\Gamma_1^1)\text{-LO}$, and $A_1'(\Gamma_1^3)$ vibrational modes of InSe, respectively (Figure 3b).^[29,30] The enhancement of the Raman signal on the pillars is stronger in the thinnest layers and is of the same order of magnitude as observed in PL (Figure 2b,c). In particular, the $A_2''(\Gamma_1^1)\text{-LO}$ mode at 201 cm^{-1} tends to be more strongly enhanced. We have observed a small shift to lower frequencies (by up to 1 cm^{-1}) of specific Raman modes (e.g., $E'(\Gamma_3^1)\text{-TO}/E''(\Gamma_3^3)$ at 176 cm^{-1} , $A_2''(\Gamma_1^1)\text{-LO}$ at 201 cm^{-1} , $A_1'(\Gamma_1^3)$ at 228 cm^{-1}) at the location of the pillars (Figure 3a, inset). These modes involve out-of-phase vibrations of the In–Se bond within each vdW layer, as sketched in Figure 3b. Thus, we assign this shift to a change of the In–Se intralayer bonds.

2.3. Modelling the Enhanced Optical Emission: Geometrical and Strain Effects

To explain our observations, we perform density functional theory (DFT) based calculations and examine the role of the geometrical shape of the flake and strain on the electronic states and light polarization properties. As shown in Figure 1, our InSe layers are tensed over the pillars with a well-defined profile described by a Gaussian with a maximum curvature $\kappa = z_0/b^2 = 7 \times 10^{-4}$ nm^{-1} . The corresponding shift of the Raman peaks (Figure 3) supports a strain-induced change of vibrational and electronic properties.^[16–25,31] The bent layers are subject to a weak tensile and compressive strain in the outer and inner surfaces, respectively, which reduces the band gap energy (Figure S5, Supporting Information). Our calculated reduction of the

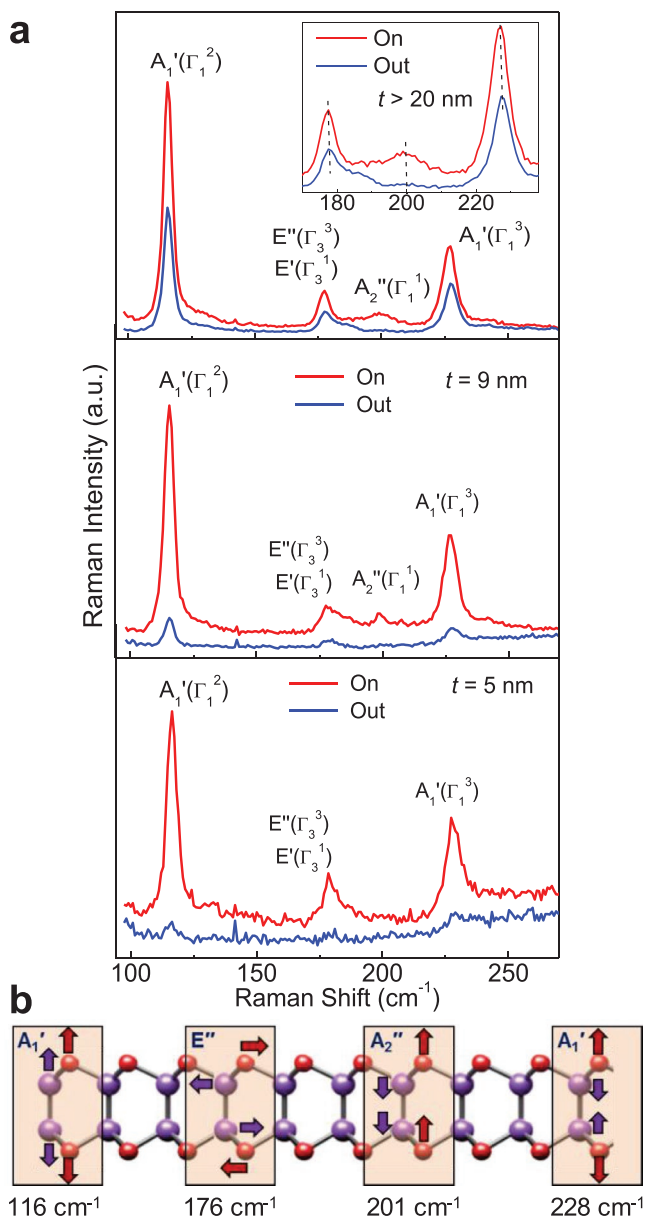


Figure 3. Enhanced Raman scattering in InSe nanoflakes on Si-pillars. a) Room temperature ($T = 300\text{K}$) Raman spectra inside and outside a Si-pillar of average height $h = 120$ nm for InSe flakes of thickness $t > 20$ nm (top), $t = 9$ nm (middle), and $t = 5$ nm (bottom). The top inset illustrates three Raman modes ($\lambda = 532$ nm, $P = 10^{-6}$ W). b) Sketch of the Raman vibrational modes measured in part (a).

band gap energy is in line with the measured energy shift (<5 meV) of the PL peak in the bent flakes. Due to the small curvature of the bent flakes, strain affects only weakly the electronic band structure. However, the geometrical shape of the flake modifies the strength of optical transitions, as discussed below.

First, we note that for unbent InSe the band edge absorption dipole couples only weakly with light polarized in the layer plane, that is, for an electric field dipole \mathbf{E} perpendicular to the c -axis ($\mathbf{E} \perp c$).^[4,14,15] Spin-orbit coupling (SOC) makes possible this coupling by mixing p_{xy} -orbitals with p_z -orbitals in the valence band.^[4] Hence, due to the preferential coupling of the

electronic states to light polarized along the c -axis, that is, for $\mathbf{E} \parallel c$, optical transitions are very sensitive to the bending of the flakes. To account for this effect, we consider a simple model for the PL emission. The relationship between the intensity of the PL signal, I_{PL} , at the band gap energy E_g and that of the exciting radiation of intensity I_{ex} and energy E_{exc} can be written as

$$I_{\text{PL}}(E_{\text{exc}}, E_g) = P_{\text{abs}}(E_{\text{exc}}) \times P_{\text{rel}}(E_{\text{exc}}, E_g) \times P_{\text{em}}(E_g) \times I_{\text{ex}}(E_{\text{exc}}) \quad (1)$$

Here, $P_{\text{abc}}(E_{\text{exc}})$ is the probability that a photon of energy E_{exc} is absorbed by the InSe layer; $P_{\text{rel}}(E_{\text{exc}}, E_g)$ is the probability that photogenerated electron-hole pairs relax toward the band edge states giving rise to emission of photons of energy E_g ; and $P_{\text{em}}(E_g)$ is the probability that photons of energy E_g are emitted after relaxation. Since $P_{\text{abs}}(E_{\text{exc}})$ and $P_{\text{em}}(E_g)$ are proportional to the absorption coefficient $\alpha(E_{\text{exc}})$ and $\alpha(E_g)$, to examine the PL intensity, we calculate the dependence of α on the photon energy, E , and on the orientation of the electric field dipole, for example, $\mathbf{E} \perp c$ and $\mathbf{E} \parallel c$. We express the optical absorption coefficient as $\alpha(E) = \frac{2\pi \text{Im}\epsilon(E)}{n\lambda}$, where $\text{Im}\epsilon$ is the imaginary part of the dielectric function, n is the refractive index, and λ is the photon wavelength. We calculate $\text{Im}\epsilon$ using first-principles calculations of the electronic band structure at highly dense k -points in the Brillouin zone with the inclusion of SOC (see Section 4).

Figure 4a,b shows the E -dependence of $\text{Im}\epsilon$ for $\mathbf{E} \perp c$ (Figure 4a) and $\mathbf{E} \parallel c$ (Figure 4b) for InSe layers of different thickness. For $\mathbf{E} \perp c$, $\text{Im}\epsilon$ increases with increasing E , more strongly for $E > 4$ eV; only a weak increase of $\text{Im}\epsilon$ can be seen at the band gap energy, E_g . For $\mathbf{E} \parallel c$ (Figure 4b), the value of $\text{Im}\epsilon$ is significantly enhanced compared to $\mathbf{E} \perp c$. To examine the absorption in the bent layers, we refer to Figure 4c, which sketches the orientation of the layers with respect to the incident light.

We define the component of the absorption coefficient coupled to light polarized in the layer plane as α^{eff} . The value of α^{eff} within ($\alpha_{\text{on}}^{\text{eff}}$) and outside ($\alpha_{\text{out}}^{\text{eff}}$) a pillar can be expressed as $\alpha_{\text{on}}^{\text{eff}} = \cos\theta\alpha_{\perp} + \sin\theta\alpha_{\parallel}$ and $\alpha_{\text{out}}^{\text{eff}} = \alpha_{\perp}$, respectively, where α_{\perp} and α_{\parallel} are the absorption coefficients for $\mathbf{E} \perp c$ and $\mathbf{E} \parallel c$, respectively, and θ is the bending angle. The value of θ for the bent flakes in Figure 1 varies from 0 to $\approx 9^\circ$. Correspondingly, the ratio $\alpha_{\text{on}}^{\text{eff}}/\alpha_{\text{out}}^{\text{eff}}$ increases from 1 for $\theta = 0$ to ≈ 3 for $\theta = 9^\circ$. To model the PL enhancement ($I_{\text{on}}/I_{\text{out}}$) on the bent flakes, we use Equation (1) and calculate I_{on} by integrating $\alpha_{\text{on}}^{\text{eff}}$ over the bent surface of the flakes. For the unbent flake, we calculate I_{out} by integrating $\alpha_{\text{out}}^{\text{eff}}$ on a flat surface with an area equals to that of the bent one. Thus, we obtain:

$$I_{\text{on}}/I_{\text{out}} = C_1 + C_2 R(E_g) R(E_{\text{exc}}) + C_3 [R(E_g) + R(E_{\text{exc}})] \quad (2)$$

where $R(E_g) = \alpha_{\parallel}(E_g)/\alpha_{\perp}(E_g)$, $R(E_{\text{exc}}) = \alpha_{\parallel}(E_{\text{exc}})/\alpha_{\perp}(E_{\text{exc}})$ and C_1 , C_2 , and C_3 are numerical coefficients (see derivation in Supporting Information, Section S5). Using Equation (2) and the calculated layer thickness dependences of $R(E_{\text{exc}})$ and $R(E_g)$ (Figure S7, Supporting Information), we derive the dependence of $I_{\text{on}}/I_{\text{out}}$ on t and E_{exc} . Due to the small curvature of the bent flakes (i.e., the bending angle, θ , for our bent flakes is always less than 9°), in the analysis of the PL intensity we neglect any change of collection efficiency of the emitted photons compared to that for unbent layers.

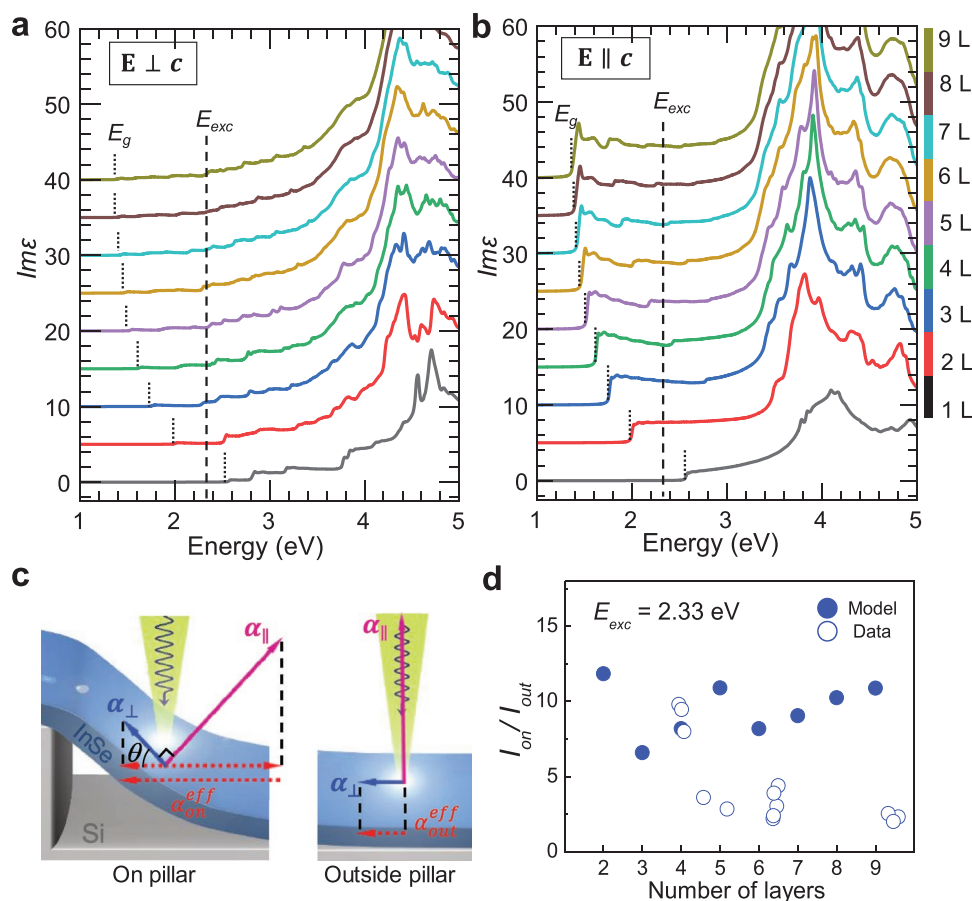


Figure 4. Modelling optical properties of bent 2D InSe. Imaginary part of the dielectric function, $\text{Im}\epsilon$, for an electric field dipole \mathbf{E} a) perpendicular and b) parallel to the c -axis. Different curves correspond to InSe layer thicknesses from $t = 1$ layer to $t = 9$ layers. The band gap energy and excitation energy are labeled as E_g and E_{exc} , respectively. c) Scheme of how the effective absorption coefficient α^{eff} for light polarized in the layer plane is enhanced on the pillar region ($\alpha_{\text{on}}^{\text{eff}}$) compared to the region outside the pillar ($\alpha_{\text{out}}^{\text{eff}}$). The values of α for $\mathbf{E} \perp c$ and $\mathbf{E} \parallel c$ are α_{\perp} and α_{\parallel} , respectively. d) Calculated and measured dependence of the photoluminescence enhancement ratio, $I_{\text{on}}/I_{\text{out}}$, on the number of InSe layers ($E_{\text{exc}} = 2.33$ eV).

Figure 4d shows the calculated value of $I_{\text{on}}/I_{\text{out}}$ for $E_{\text{exc}} = 2.33$ eV (as used in the experiment) and a range of layer thicknesses t ranging from 2 to 9 layers. Our models predict an enhancement of the PL signal, which is of the same order of magnitude as measured in our experiment. Furthermore, the corresponding enhancement of the Raman signal is in line with the larger optical absorption expected in the bent layers (S6, Supporting Information). The deviation of the model from the data for larger t may arise from the contribution of light scattering around the edges of the pillars (Figure S1, Supporting Information) and limitations of our model, which does not consider disorder effects. In particular, the band edge recombination is very sensitive to the layer thickness due to quantum confinement and strong interlayer coupling in the InSe nanosheets.^[3,32]

The PL enhancement on the bent flakes, $I_{\text{on}}/I_{\text{out}}$, depends on the photon excitation energy, E_{exc} . This can be understood by considering the dependence of $I_{\text{on}}/I_{\text{out}}$ on E_{exc} for different layer thicknesses. Figure 5a,b shows the calculated dependence of $I_{\text{on}}/I_{\text{out}}$ on E_{exc} for 2 and 4 InSe layers and the corresponding values of $\text{Im}\epsilon$ for $\mathbf{E} \parallel c$ and $\mathbf{E} \perp c$ within the same energy range. It can be seen that a strong PL enhancement is observed over

an energy range between the band gap E_g and E_2 . As shown in Figure 5c,d, E_2 corresponds to the energy of the optical transition between the CB minimum and the second VB maximum. Whereas the states of the VB maximum are made predominantly of p_z -orbitals, states from the deeper VB comprise of p_{x-y} -orbitals. Thus, optical transitions with $E_g < E_{\text{exc}} < E_2$ are most favorable for $\mathbf{E} \parallel c$ and hence most affected by bending the layers. In particular, an excitation energy from E_g to E_2 results in the strongest PL enhancement. This is realized experimentally in our 3 layers ($t = 2$ nm) InSe flake revealing a large value of $I_{\text{on}}/I_{\text{out}} = 10$ for $E_g < E_{\text{exc}} < E_2$. Thus, for a given excitation energy, the calculated PL enhancement ratio $I_{\text{on}}/I_{\text{out}}$ can exhibit a non-monotonic dependence on t (Figure 4d). This non-monotonic dependence is not observed in the experiment, suggesting that additional effects may contribute to the measured data, such as carrier relaxation processes.

The spatial modulation of the PL emission from InSe over the Si-pillars is qualitatively different from that reported for single and bi-layer TMDCs.^[33–41] In TMDCs sharp emission lines are observed at low-temperature and assigned to the recombination of excitons from localized states. These arise from crystal defects, non-homogeneous strain and/or nano wrinkles intentionally

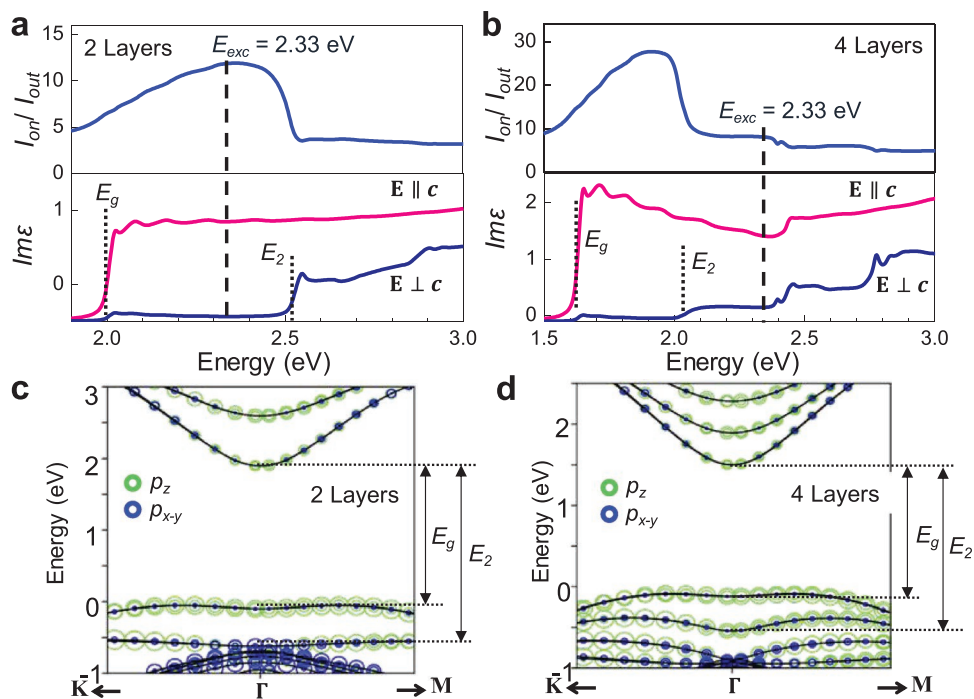


Figure 5. Photoluminescence enhancement: dependence on the photon excitation energy. a,b) Calculated photoluminescence enhancement, I_{on}/I_{out} , as a function of the photon excitation energy for a) 2 and b) 4 InSe layers and corresponding dependence of $Im\epsilon$ for $E||c$ and $E\perp c$ in the same energy range. The bandgap energy, E_g , and the energy of the optical transition between the conduction band minimum and the second valence band edge, E_2 , are indicated by black vertical dash lines. The excitation energy $E_{exc} = 2.33$ eV used in the experiment is indicated by a vertical dash line crossing all curves. c,d) Projected band structure with p_z and p_{x-y} orbitals of c) 2 and d) 4 InSe layers. The p_z and p_{x-y} orbital components are represented in green and blue, respectively. The E_g and E_2 transitions are marked by arrows.

created by exfoliating and/or transferring the TMDCs onto nanopillars, rough metallic surfaces coated with dielectrics, and/or created by intentionally structural damage of the layers. As shown in Figure 2, for InSe the modulation of the PL signal over the pillars occurs at room temperature, but the PL peak energy and linewidth do not change significantly. Thus, we exclude a dominant localization of the exciton in the layer plane due to the pillars and/or an exciton funnel effect, as observed in TMDCs.^[33]

Optical resonances can occur when light interacts with sub-wavelength dielectric cavities, as reported in WSe₂ layers coupled to dielectric nano-antennas^[42] and in vertical, small aspect-ratio and subwavelength Si-pillars.^[43] The Q-factor of the resonances depends on their morphology, geometry, and density. For our Si-pillars, the enhancement of the Raman signal from Si (≈ 1.3) (Figure S8, Supporting Information) is always smaller than that observed for the bent InSe flakes (up to a factor 10). Furthermore, the enhancement factor of both Raman and PL signals for the bent InSe flakes depends on the InSe layer thickness. Thus, we exclude that our observations arise merely from a photonic cavity effect, which could be enhanced using pillars with a different geometry and/or dielectric material.

In previous work,^[15] Gisbert et al. reported an enhanced optical emission from InSe flakes exfoliated onto agglomerates of SiO₂ nanoparticles. The measured enhancement of the optical emission was explained by the combined effect of light scattering by the nanoparticles and anisotropic light-matter interactions. Although this surface texturing approach represents a promising strategy for controlling optical signals, the use of randomly

distributed nanoparticles to texture a 2D layer is difficult to reproduce and quantify. Our data and analysis for InSe layers bent onto Si-pillars reveal that the orbital symmetry of the band-edge states and light polarization dipole selection rules play the main role in the enhancement of the optical signal. This is a reproducible effect that is strongly dependent on the geometrical shape and thickness of the bent layers. For example, the PL enhancement for flakes transferred on shorter nanopillars tend to become weaker due to the reduced bending angle (S2, Supporting Information).

3. Conclusion

In conclusion, we have demonstrated the deterministic positioning of 2D InSe flakes of different thickness onto a periodic array of Si-pillars. We have shown a reproducible bending of the layers, which causes a nanoscale spatial modulation of the Raman and photoluminescence signals across the array. DFT based calculations were used to model the measured effects and account for the role of the geometrical shape and strain of the flake on the electronic states and light polarization properties. While the strain plays a negligible role in our flakes due to their small curvature, the geometrical shape significantly modifies the integrated light emission intensity, which can be understood by taking into account the orbital symmetry of the band-edge states and light polarization dipole selection rules. Our data and analysis indicate a route toward the controlled modulation of optical properties by bending the flakes, which is

dependent on the layer thickness, optical excitation energy, and light polarization. The proposed integration of 2D InSe with Si nanostructures exploits the flexibility of this 2D material and its compatibility with Si-platforms for electronics and optoelectronics. Future developments include the transfer of the flakes onto flexible substrates with optical waveguides for the reversible modulation of optical signals and their further enhancement for specific technologies.

4. Experimental Section

Fabrication of Si-Pillars: The Si-pillars were fabricated by EBL and dry etching on 4-inch Si(100) wafers. Following the spin coating of e-beam resist (ZEP520A diluted with ZEP-A by a volume ratio of 2:1) and e-beam writing, the resist was developed using a ZED N-50 developer. Then, the Si substrate was etched using an inductively coupled plasma etcher (Oxford 80Plus) by flowing 10 sccm of SF₆, 25 sccm of CHF₃, and 2 sccm of O₂. The RF power and the chamber pressure for the dry etching were set to 200 W and 30 mTorr, respectively. After the etching, the resist was removed by cleaning with *N*-methylpyrrolidone at 80 °C, followed by isopropyl alcohol rinsing, and N₂ blow-drying.

Exfoliation and Dry Transfer of InSe Flakes: The γ -polytype InSe crystal was grown using the Bridgman method from a polycrystalline melt of In_{1.03}Se_{0.97}. The crystal structure was probed by X-ray diffraction using a DRON-3 X-ray diffractometer in a monochromatic Cu-K α radiation of wavelength $\lambda = 1.5418$ Å. The γ -phase of the InSe bulk crystals and thin layers was further assessed by Raman spectroscopy studies.^[3] The InSe nanosheets were prepared from the as-grown crystals by mechanical exfoliation. A two-step approach was used in which the flakes were first thinned down with the aid of F07 backgrinding tape from Microworld and then transferred onto a PDMS film on a glass slide. This was followed by dry-transfer of individual flakes onto the Si-pillars.

Microscopy and Optical Studies: The topography of the flakes was examined by SEM using a JEOL-JSM-6610LV. AFM images were also acquired in the tapping mode under ambient conditions using an asylum research MFP-3D. The experimental set-up for the μ PL and μ Raman spectroscopy studies at room temperature comprised a He-Ne laser ($\lambda = 633$ nm) and a frequency doubled Nd:YVO₄ laser ($\lambda = 532$ nm), an x-y-z motorized stage and an optical confocal microscope system equipped with a 0.5 m long monochromator with 150 and 1200 g mm⁻¹ gratings. For experiments at $T = 8$ K, the sample was placed on the cold finger of a continuous gas flow cryostat mounted on an x-y-z motorized stage. The laser beam was focused to a diameter $d = 1$ μ m using 50 \times or 100 \times objectives. The PL signal was detected by a Si-charge-coupled device (CCD) camera. Thermal- and photo-annealing in air can induce an oxidation of the InSe surface, which converts a few surface layers of InSe into In₂O₃.^[44] Thus, PL experiments were performed at low excitation power ($P \leq 0.1$ mW) to avoid excessive heating and surface degradation. Also, experiments were conducted on several samples and the reproducibility of the data assessed by multiple studies.

First-Principles Modelling: First-principles calculations were carried out within the framework of DFT by using the plane-wave pseudopotential approach as implemented in the VASP code.^[45,46] The generalized gradient approximation formulated by Perdew, Burke, and Ernzerhof^[47] was used as exchange-correlation functional. The electron-ion interactions were described by using the projected augmented wave pseudopotentials with the 5s²5p¹(In), 4s²4p⁴(Se) treated explicitly as valence electrons. The kinetic energy cutoff for the plane wave basis was chosen to be 500 eV, with k -point grid spacing set to $2\pi \times 0.03$ Å⁻¹ for electronic Brillouin zone integration. To simulate multiple InSe layers, a vertical vacuum space with the thickness of 15 Å or more were adopted to separate the layers from their periodic images. The interlayer distance was optimized through total energy minimization including the vdW interaction using the optB86b-vdW functional,^[48] with the residual forces on the atoms converged to below 0.05 eV Å⁻¹. For the optical studies

requiring refined Brillouin zone sampling, extremely dense Γ -centered k -points mesh of $48 \times 48 \times 1$, $40 \times 40 \times 1$, $36 \times 36 \times 1$ and $32 \times 32 \times 1$ were used for 1–5 layers, 6–7 layers, 8 and 9 layers, respectively. To remedy the band gap underestimation issue of DFT, a scissor operator with a magnitude equal to the band gap energy difference between the value calculated by DFT and that one from the measured PL was used. Spin-orbital coupling was included. This introduced a significant change to the orbital composition of the electronic states near the band edge, thus affecting optical transitions.

Supporting Information

Supporting Information is available from the Wiley Online Library or from the author.

Acknowledgements

D.M. and J.X. contributed equally to this work. This work was supported by the Defense Science and Technology Laboratory (DSTL); the Engineering and Physical Sciences Research Council (grant number EP/M012700/1); the European Union's Horizon 2020 research and innovation programme Graphene Flagship Core 3; The National Academy of Sciences of Ukraine; The Leverhulme Trust (RF-2017-224); The Royal Society (IE160395). A.P. acknowledges the Chinese Academy of Sciences (CAS) for the award of a "President's International Fellowship for Visiting Scientists". The work at Jilin University was supported by the National Natural Science Foundation of China (Grant No. 61722403 and 11674121), Jilin Province Science and Technology Development Program (Grant No. 20190201016[C]). Calculations were performed in part at the high performance computing center of Jilin University.

Conflict of Interest

The authors declare no conflict of interest.

Keywords

2D excitons, enhanced luminescence, indium selenide, Si pillars

Received: May 20, 2020

Published online:

- [1] K. Novoselov, A. Mishchenko, A. Carvalho, A. H. Neto, *Science* **2016**, 353, aac9439.
- [2] N. Mounet, M. Gibertini, P. Schwaller, D. Campi, A. Merkys, A. Marrazzo, T. Sohier, I. E. Castelli, A. Cepellotti, G. Pizzi, N. Marzari, *Nat. Nanotechnol.* **2018**, 13, 246.
- [3] G. W. Mudd, S. A. Svatek, T. Ren, A. Patanè, O. Makarovskiy, L. Eaves, P. H. Beton, Z. D. Kovalyuk, G. V. Lashkarev, Z. R. Kudrynskiy, A. I. Dmitriev, *Adv. Mater.* **2013**, 25, 5714.
- [4] M. B. Gisbert, R. Proux, R. Picard, D. A. Penares, A. Branny, A. M. Sánchez, J. F. Sánchez-Royo, B. D. Gerardot, *Nat. Commun.* **2019**, 10, 3913.
- [5] G. W. Mudd, M. R. Molas, X. Chen, V. Zólyomi, K. Nogajewski, Z. R. Kudrynskiy, Z. D. Kovalyuk, G. Yusa, O. M. L. Eaves, M. Potemski, V. I. Fal'ko, A. Patanè, *Sci. Rep.* **2016**, 6, 39619.
- [6] D. A. Bandurin, A. V. Tyurnina, G. L. Yu, A. Mishchenko, V. Zólyomi, S. V. Morozov, R. K. Kumar, R. V. Gorbachev, Z. R. Kudrynskiy,

- S. Pezzini, Z. D. Kovalyuk, U. Zeitler, K. S. Novoselov, A. Patané, L. Eaves, I. V. Grigorieva, V. I. Fal'ko, A. K. Geim, Y. Cao, *Nat. Nanotechnol.* **2017**, *12*, 223.
- [7] J. F. Sánchez-Royo, G. M. Matutano, M. B. Gisbert, J. P. M. Pastor, A. Segura, A. Cantarero, R. Mata, J. Canet-Ferrer, G. Tobias, E. Canadell, J. Marqués-Hueso, B. D. Gerardot, *Nano Res.* **2014**, *7*, 1556.
- [8] S. R. Tamalampudi, Y. Y. Lu, R. Kumar, R. Sankar, C. D. Liao, K. Moorthy B, C. Cheng, F. C. Chou, Y. T. Chen, *Nano Lett.* **2014**, *14*, 2800.
- [9] G. W. Mudd, S. A. Svatek, L. Hague, O. Makarovskiy, Z. R. Kudrynskiy, C. J. Mellor, P. H. Beton, L. Eaves, K. S. Novoselov, Z. D. Kovalyuk, E. E. Vdovin, A. J. Marsden, N. R. Wilson, A. Patané, *Adv. Mater.* **2015**, *27*, 3760.
- [10] F. Yan, L. Zhao, A. Patané, P. Hu, X. Wei, W. Luo, D. Zhang, Q. Lv, Q. Feng, C. Shen, K. Chang, L. Eaves, K. Wang, *Nanotechnology* **2017**, *28*, 27LT01.
- [11] M. A. Bhuiyan, Z. R. Kudrynskiy, D. Mazumder, J. D. G. Greener, O. Makarovskiy, C. J. Mellor, E. E. Vdovin, B. A. Piot, I. I. Lobanova, Z. D. Kovalyuk, M. Nazarova, A. Mishchenko, K. S. Novoselov, Y. Cao, L. Eaves, G. Yusa, A. Patané, *Adv. Funct. Mater.* **2019**, *29*, 1805491.
- [12] W. Feng, W. Zheng, W. Cao, P. Hu, *Adv. Mater.* **2014**, *26*, 6587.
- [13] M. Hamer, E. Tóvári, M. Zhul, M. Thompson, A. Mayorov, J. Prance, Y. Lee, R. P. Haley, Z. R. Kudrynskiy, A. Patané, D. Terry, Z. D. Kovalyuk, K. Ensslin, A. V. Kretinin, A. Geim, R. Gorbachev, *Nano Lett.* **2018**, *18*, 3950.
- [14] M. Brotons-Gisbert, D. Andres-Penares, J. Suh, F. Hidalgo, R. Abargues, P. J. Rodríguez-Cantó, A. Segura, A. Cros, G. Tobias, E. Canadell, P. Ordejón, J. Wu, J. P. Martínez-Pastor, J. F. Sánchez-Royo, *Nano Lett.* **2016**, *16*, 3221.
- [15] Y. Li, T. Wang, H. Wang, Z. Li, Y. Chen, D. West, R. Sankar, R. K. Ulaganathan, F. Chou, C. Wetzel, C. Xu, S. Zhang, S. Shi, *Nano Lett.* **2018**, *18*, 5078.
- [16] M. Wu, J. Shi, M. Zhang, Y. Ding, H. Wang, Y. Cena, J. Lua, *Nanoscale* **2018**, *10*, 11441.
- [17] Y. Li, T. Wang, M. Wu, T. Cao, Y. Chen, R. Sankar, R. K. Ulaganathan, F. Chou, C. Wetzel, C. Xu, *2D Mater.* **2018**, *5*, 021002.
- [18] Y. Ma, Y. Dai, L. Yu, C. Niu, B. Huang, *New J. Phys.* **2013**, *15*, 073008.
- [19] Y. Li, X. Niu, J. Wang, *FlatChem* **2019**, *15*, 100092.
- [20] Y. Li, C. Yu, Y. Gan, Y. Kong, P. Jiang, D. Zou, P. Li, X. Yu, R. Wu, H. Zhao, C. Gao, J. Li, *Nanotechnology* **2019**, *30*, 335703.
- [21] D. Akinwande, N. Petrone, J. Hone, *Nat. Commun.* **2014**, *5*, 5678.
- [22] C. Lee, X. Wei, J. W. Kysar, J. Hone, *Science* **2008**, *321*, 385.
- [23] M. Yagmurcukardes, R. Senger, F. Peeters, H. Sahin, *Phys. Rev. B* **2016**, *94*, 245407.
- [24] Q. Zhao, R. Frisenda, T. Wang, A. Castellanos-Gomez, *Nanoscale* **2019**, *11*, 9845.
- [25] Q. Wang, L. Han, L. Wu, T. Zhang, S. Li, P. Lu, *Nanoscale Res. Lett.* **2019**, *14*, 287.
- [26] G. W. Mudd, A. Patané, Z. R. Kudrynskiy, M. W. Fay, O. Makarovskiy, L. Eaves, Z. D. Kovalyuk, V. Zólyomi, V. Falko, *Appl. Phys. Lett.* **2014**, *105*, 221909.
- [27] J. Martínez-Pastor, A. Segura, C. Julien, A. Chevy, *Phys. Rev. B* **1992**, *46*, 4607.
- [28] C. Ferrer-Roca, A. Segura, M. Andrés, J. Pellicer, V. Muñoz, *Phys. Rev. B* **1997**, *55*, 6981.
- [29] N. Kuroda, Y. Nishina, *Solid State Commun.* **1978**, *28*, 439.
- [30] S. Lei, L. Ge, S. Najmaei, A. George, R. Kappera, J. Lou, M. Chhowalla, H. Yamaguchi, G. Gupta, R. Vajtai, A. D. Mohite, P. M. Ajayan, *ACS Nano* **2014**, *8*, 1263.
- [31] C. Song, F. Fan, N. Xuan, S. Huang, G. Zhang, C. Wang, Z. Sun, H. Wu, H. Yan, *ACS Appl. Mater. Interfaces* **2018**, *10*, 3994.
- [32] Y. Sun, S. Luo, X. Zhao, K. Biswas, S. Li, L. Zhang, *Nanoscale* **2018**, *10*, 7991.
- [33] A. Branny, S. Kumar, R. Proux, B. D. Gerardot, *Nat. Commun.* **2017**, *8*, 15053.
- [34] C. Palacios-Berraquero, D. M. Kara, A. R. P. Montblanch, M. Barbone, P. Latawiec, D. Yoon, A. K. Ott, M. Loncar, A. C. Ferrari, M. Atatüre, *Nat. Commun.* **2017**, *8*, 15093.
- [35] P. Tonndorf, R. Schmidt, R. Schneider, J. Kern, M. Buscema, G. A. Steele, A. Castellanos-Gomez, H. S. J. Zant, S. Vasconcellos, R. Bratschkitsch, *Optica* **2015**, *2*, 347.
- [36] O. Iff, N. Lundt, S. Betzold, L. N. Tripathi, M. Emmerling, S. Tongay, Y. J. Lee, S. Kwon, S. Höfling, C. Schneider, *Opt. Express* **2018**, *26*, 25944.
- [37] L. N. Tripathi, O. Iff, S. Betzold, Ł. Dusanowski, M. Emmerling, K. Moon, Y. J. Lee, S. Kwon, S. Höfling, C. Schneider, *ACS Photonics* **2018**, *5*, 1919.
- [38] Y. Luo, G. D. Shepard, J. V. Ardelean, D. A. Rhodes, B. Kim, K. Barmak, J. C. Hone, S. Strauf, *Nat. Nanotechnol.* **2018**, *13*, 1137.
- [39] T. Cai, J. Kim, Z. Yang, S. Dutta, S. Aghaeimeibodi, E. Waks, *ACS Photonics* **2018**, *5*, 3466.
- [40] J. Chaste, A. Missaoui, S. Huang, H. Henck, Z. B. Aziza, L. Ferlazzo, A. Balan, A. T. C. Johnson, R. Braive, A. Ouerghi, *ACS Nano* **2018**, *12*, 3235.
- [41] S. Kumar, A. Kaczmarczyk, B. D. Gerardot, *Nano Lett.* **2015**, *15*, 7567.
- [42] L. Sortino, P. G. Zotev, S. Mignuzzi, J. Cambiasso, D. Schmidt, A. Genco, M. Aßmann, M. Bayer, S. A. Maier, R. Sapienza, A. I. Tartakovskii, *Nat. Commun.* **2019**, *10*, 5119.
- [43] F. J. Bezares, J. P. Long, O. J. Glembocki, J. Guo, R. W. Rendell, R. Kasic, L. Shirey, J. C. Owrutsky, J. D. Caldwell, *Opt. Express* **2013**, *21*, 27587.
- [44] N. Balakrishnan, Z. R. Kudrynskiy, E. F. Smith, M. W. Fay, O. Makarovskiy, Z. D. Kovalyuk, L. Eaves, P. H. Beton, A. Patane, *2D Mater.* **2017**, *4*, 025043.
- [45] G. Kresse, J. Furthmüller, *Comput. Mater. Sci.* **1996**, *6*, 15.
- [46] G. Kresse, J. Furthmüller, *Phys. Rev. B* **1996**, *54*, 11169.
- [47] J. P. Perdew, K. Burke, M. Ernzerhof, *Phys. Rev. Lett.* **1996**, *77*, 3865.
- [48] J. Klimeš, D. R. Bowler, A. Michaelides, *J. Phys.: Condens. Matter* **2010**, *22*, 022201.